Dynamic analysis of TMT

Douglas G. MacMynowski, Carl Blaurock, George Z. Angeli

Douglas G. MacMynowski, Carl Blaurock, George Z. Angeli, "Dynamic analysis of TMT," Proc. SPIE 7017, Modeling, Systems Engineering, and Project Management for Astronomy III, 70170W (9 July 2008); doi: 10.1117/12.786935

SPIE.

Event: SPIE Astronomical Telescopes + Instrumentation, 2008, Marseille, France

Dynamic Analysis of TMT

Douglas G. MacMynowski[a], Carl Blaurock[b] and George Z. Angeli[c]

[a]California Institute of Technology
Department of Control and Dynamical Systems, Pasadena CA 91125
[b]NightSky Systems Inc., Raleigh, NC 27616
[c]Thirty Meter Telescope Observatory, Pasadena, CA 91125

ABSTRACT

Dynamic disturbance sources affecting the optical performance of the Thirty Meter Telescope (TMT) include unsteady wind forces inside the observatory enclosure acting directly on the telescope structure, unsteady wind forces acting on the enclosure itself and transmitted through the soil and pier to the telescope, equipment vibration either on the telescope itself (e.g. cooling of instruments) or transmitted through the soil and pier, and potentially acoustic forces. We estimate the characteristics of these disturbance sources using modeling anchored through data from existing observatories. Propagation of forces on the enclosure or in support buildings through the soil and pier to the telescope base are modeled separately, resulting in force estimates at the telescope pier. We analyze the resulting optical consequences using integrated modeling that includes the telescope structural dynamics, control systems, and a linear optical model. The dynamic performance is given as a probability distribution that includes the variation of the external wind speed and observing orientation with respect to the wind, which can then be combined with dome seeing and other time- or orientation-dependent components of the overall error budget. The modeling predicts acceptable dynamic performance of TMT.

Keywords: Extremely Large Telescopes, Performance Modeling, Wind Buffeting, Vibration

1. INTRODUCTION

The Thirty Meter Telescope (TMT) is being designed to stringent image performance requirements. One source of image degradation is due to dynamic (time-varying) forces on the telescope, where the time-scale is sufficiently fast so that quasi-steady analysis is insufficient, and the interaction with the control system and structural dynamics must be accounted for in predicting the optical consequences. There are three sources in particular that we consider herein: wind, equipment vibration, and acoustic forces. Of these, wind is the most significant, and thus most of the paper is devoted to the analysis of the response due to wind forces.

TMT will operate in both seeing-limited and adaptive-optics (AO) modes. The overall performance goal in the seeing-limited regime is for the telescope to degrade observing by no more than 10% relative to a perfect telescope; this is specified in terms of the normalized Point Source Sensitivity (PSSn), described in [1]. With adaptive optics on, there is a similarly stringent specification on the wavefront error uncorrectable by AO so that the telescope itself does not significantly limit the achievable performance. These requirements are then allocated to the various contributions; the allocation for dynamic errors is $\mathrm{PSSn} > 0.9959$ and uncorrectable wavefront error $\mathrm{WFE} < 14\,\mathrm{nm}$. In addition, rms vibration-induced image motion is required to be less than 36 nm (1 mas). Because many of the contributions to image degradation vary depending on observing zenith angle, external wind speed and orientation, and other factors, it is essential to capture not just the median or worst-case performance, but the probability distribution (pdf) of the performance over observing conditions. Furthermore, these external variations introduce correlations between different contributions to the TMT error budget, e.g. wind-buffeting and mirror/dome-seeing both depend on the external wind speed. Thus while herein we present the dynamic contributions to the performance estimate, the complete performance estimate combines multiple contributions through a Monte Carlo (standard year) approach.[2]

Uncorrelated effects can of course be separately predicted. Indeed, the model elements relevant to predicting one effect are not necessarily those relevant to predicting another. Thus we do not require a single piece of software that simultaneously predicts every dynamic effect, but rather tailor modeling software to the particular problem and combine effects only where it reduces analysis effort. Two related models are used herein.

First, an integrated model described previously[3] that combines (i) the TMT structural dynamic model, obtained from Finite Element Modeling (FEM),[4] (ii) dynamically accurate mount control laws[5] and a sufficiently accurate representation of other relevant active optics control loops, (iii) a linear optical model[6] and (iv) a

Modeling, Systems Engineering, and Project Management for Astronomy III, edited by George Z. Angeli, Martin J. Cullum, Proc. of SPIE Vol. 7017, 70170W, (2008) · 0277-786X/08/$18 · doi: 10.1117/12.786935

frequency-domain disturbance model that includes a parametric description of wind forces.[7] In addition to the wind forces applied to the telescope structure at the top end and on the primary mirror (M1), the effects of wind loads on the enclosure itself are applied at the telescope pier, and vibration forces are applied at multiple locations. The analysis of the transmission of wind loads or vibrations from the enclosure through the soil to the pier is conducted with a separate FEM.[8] This integrated model captures the telescope image motion and low spatial frequency image blur due to optics misalignment or large-scale deformation of M1.

The second model used herein is designed to capture the full M1 dynamic segment response due to wind; principally the inter-segment discontinuities that are uncorrectable by AO. Simplifications are made in the representation of telescope structural dynamics in order to make this model computationally tractable. The primary mirror control system (M1CS) effects are included, however there is no need to capture the dynamics that limit the M1CS bandwidth. The achievable bandwidth is separately predicted with a dedicated computationally-efficient model described in [9]. Once the primary mirror response due to wind disturbances is known, the wavefront error uncorrectable by AO is computed through AO-specific modeling.

The relationship between these two models, and related tools, is shown schematically in Fig. 1. Similar tools have also been developed for other projects.[10]

This paper is organized as follows. As noted, the wind forces are the most significant dynamic contributor to image degradation. The next sections describe first the wind forces and sources of knowledge about the wind loads, second the modeling tools and response for image jitter and low wavenumber image blur, and third the modeling tools and response for M1 segment dynamic response. The vibration and acoustic disturbances are covered in Sec. 5.

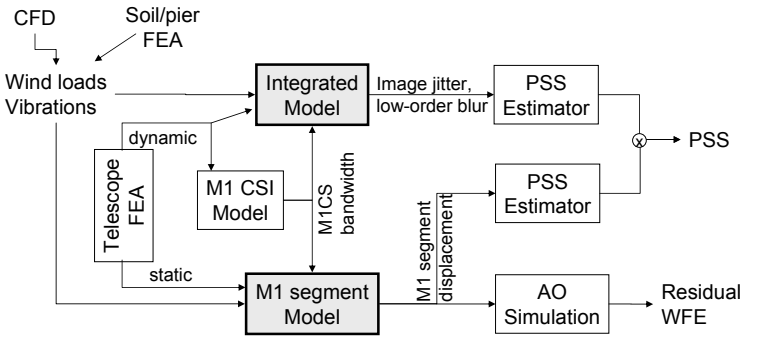

Figure 1. Relationship between models. The two models described herein are shaded, corresponding to low and high wavenumber responses. The output of these is converted to PSS, with the high wavenumber (M1 segment) response also used in AO simulations. Additional modeling tools are described in related papers (see text).

2. WIND LOADS

2.1 Overview

The strategy taken by TMT in minimizing wind response is to (i) minimize the wind speeds at the telescope top end both by minimizing the open aperture area through the choice of Calotte enclosure design, and the addition of flaps around the aperture to deflect the shear layer,[11] (ii) minimize the telescope upper-end cross-section to minimize loads, and (iii) maximize mount control system (MCS) bandwidth. With these design strategies we predict that TMT will have less wind-induced image jitter than typical existing telescopes.

In order to minimize mirror and dome-seeing due to thermal variations, the TMT enclosure is vented. At very low external wind speeds, the vents will be fully open ($\beta = 1$); at high external wind speeds they will be fully closed ($\beta = 0$), and in between the fractional opening β can be chosen to obtain a target wind speed across M1. The choice of target wind speed is based on a trade-off between wind-induced performance and mirror- and dome-seeing; we will present results for 1 and 1.25 m/s. We also require $\beta \geq 0.075$ for upwind orientations to avoid amplification of shear layer modes, and $\beta \geq 1/U_\infty$ to ensure a minimum of 10 air exchanges per hour.

Unsteady wind forces due to turbulence inside the enclosure are most significant on the upper telescope structure and on the primary mirror. The former predominantly influences telescope pointing through the resultant torque, while the latter results in both image motion and higher-order M1 deformation that contributes to both seeing-limited and AO-relevant performance. Wind loads on the enclosure can also be transmitted through the soil to result in telescope image motion, however the analysis herein indicates that this is a much less significant effect. A detailed description of wind modeling and sources can be found in [7]; here we briefly summarize key points, differences from that model, and provide additional detail on orientation dependence.

Knowledge of wind loads comes from data collected at Gemini and Keck, two wind-tunnel tests, and extensive use of computational fluid dynamics (CFD), validated by the experimental data. The basic approach taken by TMT is to estimate the reduction in wind speed inside the enclosure relative to the external wind speed, and estimate forces from the drag coefficient C_D and dynamic pressure $q = \frac{1}{2}\rho u_{\text{eff}}^2$. The relevant effective velocity

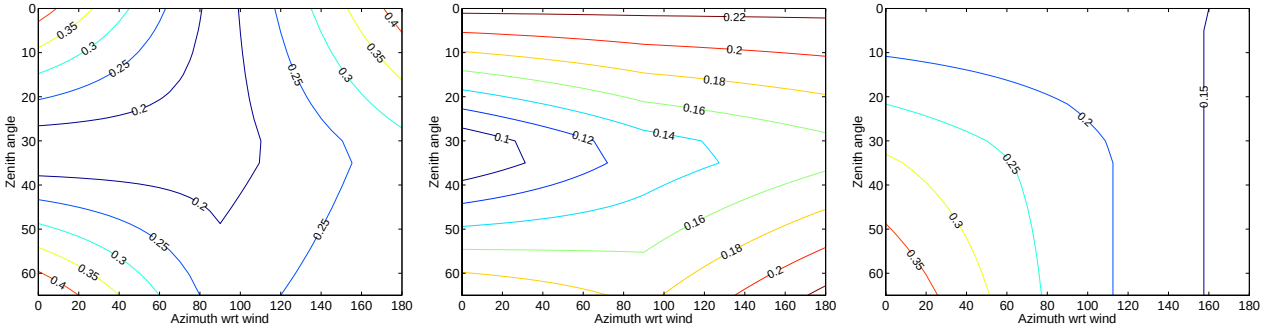

Figure 2. CFD results: Effective wind speed as a fraction of external velocity at top end, vents open (left) and closed (center), and over M1, vents open (right). With vents closed, the wind over M1 is small at all orientations.

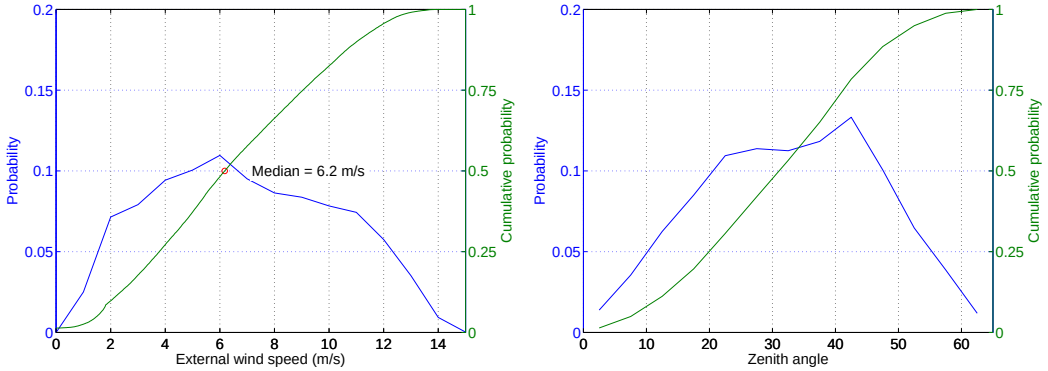

Figure 3. Probability distribution for factors influencing wind-buffeting response. External wind speed pdf (left) and assumed observing zenith angle pdf (right).

$u_{\rm eff}$ is defined in order to predict the unsteady pressure, and depends on the mean ($\bar{u}$) and rms velocity ($u_{\rm rms}$) as $u_{\rm eff}^2 = \sqrt{(2\bar{u}u_{\rm rms})^2 + 2u_{\rm rms}^4}$. For simplicity (recognizing that the exact characteristics are dependent on design and site details), we estimate $u_{\rm eff}$ from CFD only at the telescope top end and at M1, and interpolate for locations in between. Similarly, CFD is conducted for vents fully open or vents closed, and interpolated in between.

A full description of the wind loads on the telescope requires (i) a probabilistic description of the external environment (orientation, wind speed), (ii) $u_{\rm eff}$ as a function of orientation with respect to the wind, (iii) the wind force temporal spectrum, combining the pressure spectrum and spatial decorrelation effects, and (iv) a description of the structural cross-section and drag-coefficients.

2.2 External environment & orientation dependence

The external wind speed probability distribution for the TMT baseline site of Armazones is shown in Fig. 3. The wind speeds for other sites considered are slightly lower. A detailed description of observing angle with respect to wind direction is considered in [2]; here we consider only the zenith angle distribution, also given in Fig. 3, and assume a uniform probability distribution of azimuth angle with respect to the wind.

The dependence of $u_{\rm eff}$ on telescope orientation, computed from CFD,[11] is shown in Fig. 2. A representative CFD simulation from which this information is extracted is shown in Fig. 4. Combining the orientation dependence with the probability distribution of orientation and external wind speed gives the expected probability distribution of wind speed at M1 and the top-end, and the distribution of vent opening, shown in Fig. 5.

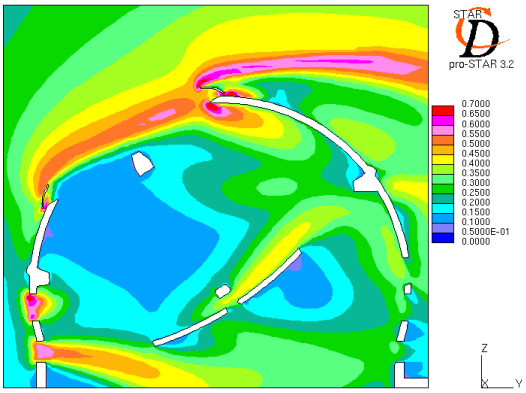

Figure 4. CFD simulation of $u_{\rm eff}/u_\infty$ at 0° azimuth, 32.5° zenith angle. The telescope top end is below the shear layer.

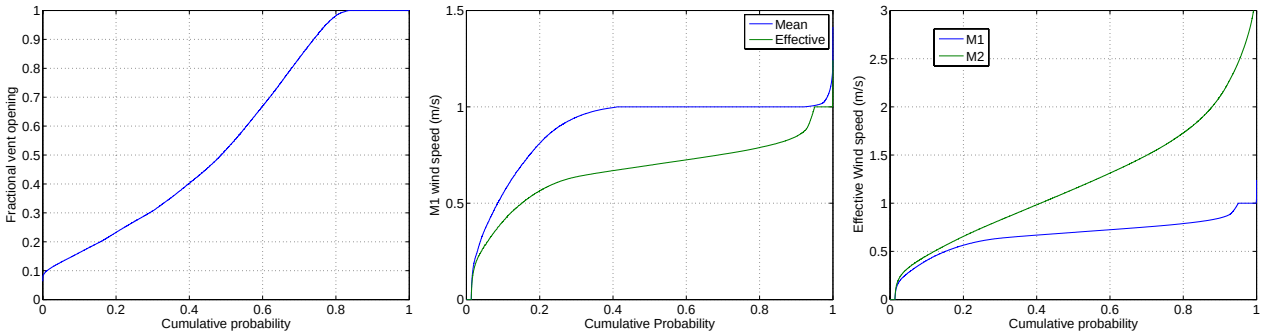

Figure 5. Probability distribution for vent fractional open area (left), mean and effective wind speed at M1 (centre) and internal wind speeds u_{eff} at M1 and top end (labeled 'M2'), all for 1 m/s target M1 wind speed.

2.3 Wind spectrum and decorrelation

The spectrum of the wind unsteady velocity or pressure is assumed to be von Karman throughout the enclosure. While the turbulence is certainly not isotropic and fully developed, nonetheless measurements at Gemini, in wind-tunnel tests, and in unsteady CFD all indicate that this is a good assumption.[7] The outer scale is based on the source of turbulence; the aperture diameter $D = 31.25$ m for turbulence created by flow passing through or over the aperture, or the vent height $H = 5$ m for turbulence generated by flow through the vents. In previous analyses, we approximated the pressure spectrum on M1 with a single outer scale interpolated between these by the fraction of turbulent energy expected from the two sources; here we explicitly retain both components of turbulence so that the spectrum is of the form

$$\Phi_p(f) \propto \alpha_0 \frac{1/f_0}{(1+(f/f_0)^2)^{7/6}} + \alpha_1 \frac{1/f_1}{(1+(f/f_1)^2)^{7/6}} \tag{1}$$

with $f_0 = U/D$, $f_1 = U/H$, and U the local mean velocity. At the telescope top end, $\alpha_1 = 0$ while over M1 the ratio α_1/α_0 depends on the vent opening β.

There may also be a small amount of turbulence with larger outer scale due to external atmospheric turbulence; Gemini data suggests that this is small and since it is at low frequencies where the control system has higher gain, we ignore this effect. Flow passing over telescope structure, instruments, etc., will result in additional turbulence introduced by these interactions that is not captured in simplified wind-tunnel geometries. There is some evidence for this effect in a few data sets at Gemini, which gives an upper bound of about 25% of the total energy on how large this additional introduced turbulence could be. To accurately capture the effects of turbulence at high wavenumber on M1, we introduce additional turbulence with an outer scale associated with representative telescope structural dimensions of 1–2 m.

Eq. (1) gives the pressure spectrum at a point, but it is the force spectrum that we are interested in. The spatial decorrelation of pressure is frequency dependent, introducing an additional rolloff in the force spectrum that depends on the structural length scale.[7] At low frequencies, the pressure across a structure of length L is correlated. At high frequencies, there are n independent turbulent structures along the length which add in quadrature rather than linearly. At frequency f, $n = aLf/U$ where the ratio of wavelength to correlation length is $a \simeq 2$ (see Appendix). This gives a corner frequency for the additional roll-off of $f_s = U/(aL)$. For computing the effect on a rounded structure such as the telescope top end or the enclosure, most of the drag force is produced over the central portion of the projected cross-sectional area, and the relevant factor a to use is smaller. The correct value has not been quantified through experiment or simulation, but herein we use $a = 1$. For estimating forces on M1, the pressure is projected onto a Zernike basis, and the relevant decorrelation length-scale depends on Zernike radial degree.[7]

The spatial decorrelation has a *significant* effect on the predicted image motion and also on which forces are most relevant. The telescope response is highest for torques applied about the elevation axis, and the peak sensitivity is near the elevation mount control bandwidth of 0.5 Hz. At this frequency, and for a representative 2 m/s internal wind speed, the forces on the roughly 3 m×3 m top end are still mostly correlated, while the force on a 20 m structural member is reduced by a factor of ∼3 relative to what would be predicted from its projected

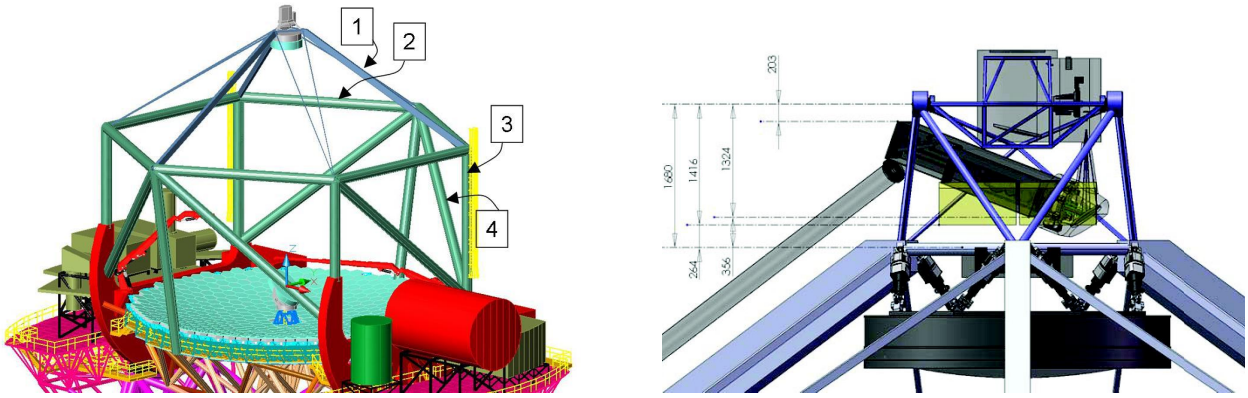

Figure 6. Left: TMT upper structure. Numbers refer to groups of members used in Table 1. Right: Detail on top end.

Group	Moment arm H (m)	Length L (m)	Width W (m)	C_D	number n	$HLWC_D\sqrt{n}$ (Nm/Pa)	Relative contribution to IJ variance
Top end	25	$10\,\mathrm{m}^2$		1.5	1	375	63%
1	20	13.5	0.66	2	3	614	26%
2	14.4	15.5	1	1.2	4	536	10%
3	7.2	14.4	1	1.3	6	322	$< 1\%$
4	7.2	23	1	1.2	6	487	1%

Table 1. Upper structure cross-sectional area and characteristics. The length includes the projection with respect to wind. The product $HLWC_D\sqrt{n}$ gives the expected torque per unit dynamic pressure without decorrelation effects. The relative contribution of each group of members to the non-M1-source image jitter (IJ) is computed from the model described in the next sections, at 60° zenith angle, 0° azimuth, and a 82.5^{th} percentile external wind speed of 10 m/s.

area alone. Furthermore, both wind speeds and the moment arm about the elevation axis decrease further inside the dome. The top-end structure itself thus remains the dominant contributor to wind-induced image motion at high external wind speeds (the torque due to the desired wind speed on M1 may result in higher image motion at low external wind speed).

2.4 TMT wind cross-section

This discussion leads directly into the final component required for estimating the wind forces on the telescope structure; the projected area and drag coefficients (or pressure coefficient for M1). Figure 6 illustrates the structural design, and the area, C_D, and moment arm for different components is tabulated in Table 1. Because the dominant effect on TMT performance due to forces on the support structure is the image motion caused by the compliance of the elevation-axis mount control in response to torque about the elevation axis, the forces estimated on the elevation structure members are represented in simulation by an equivalent force on the top end that produces the same torque.

To predict forces on M1, the analogous factor to the drag coefficient is the pressure coefficient; the ratio of the dynamic pressure to the pressure exerted on the mirror surface. From Bernoulli $C_p = 1$; there would be a deviation if we instead referenced the local pressure to the air speed away from the mirror, as was true for instance in data collected at Gemini. The wind speeds behind M1 will be significantly lower due to the blockage effects of the support structure, and thus the back surface does not contribute significantly to the net force.

2.5 Enclosure forces

The wind forces on the telescope enclosure have been predicted for a single orientation from CFD, plotted in Fig. 7. The dominant unsteady forces are not due to the turbulence in the incoming air, but rather from von Karman shedding off the enclosure at a Strouhal number of ∼0.33 (frequency $0.33U_\infty/D_d$). This shedding then leads to additional broadband turbulence. At a 10 m/s external wind, the unsteady wind forces on the TMT enclosure are roughly 10 kN in the wind direction and 25 kN in the orthogonal direction. The moments are accurately captured if the unsteady wind force is applied 20 m above the ground. Note that the unsteady CFD produces non-realistic extra turbulence at high frequencies. The spectrum we use assumes von Karman turbulence with additional attenuation due to the spatial decorrelation described earlier.

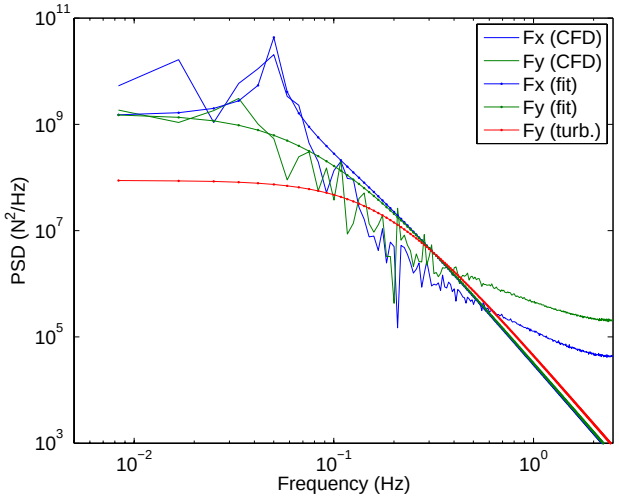

Figure 7. Force spectrum on enclosure at 10 m/s external wind, from CFD, and fit. The peak in F_x (orthogonal to wind) at 0.05 Hz is due to von Karman shedding. The CFD is known to produce excessive high-frequency turbulence.

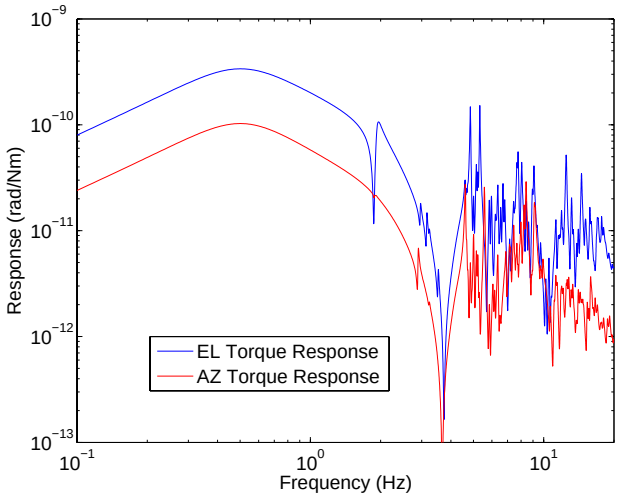

Figure 8. Mount control torque response. The peak response is to disturbances near 0.5 Hz. Note that the azimuth response is significantly lower than the elevation response for equal torques, due to the higher inertia.

A separate finite element soil model has been used to propagate the enclosure wind forces through to motion at the telescope pier.[8] At low frequencies, the propagation transfer function is roughly constant. For estimated soil properties, the pier displacement in the direction of the applied force is 10^{-11} m/N and rotation 1.5×10^{-13} rad/N.

3. WIND-INDUCED IMAGE JITTER AND LOW-ORDER ABERRATIONS

3.1 Integrated Modeling

As noted earlier, the response of TMT to wind forces is separated into low order (mostly image jitter due to telescope pointing) and high-order (M1 segment dephasing) effects. These are separately predicted, using the models discussed here and in the next section. The TMT integrated model, depicted in Fig. 9, is discussed in [3] and will only be briefly summarized here. The performance is evaluated in the frequency domain, and hence all responses are assumed to be linear.

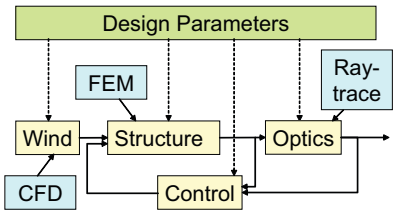

Figure 9. Information flow in parametric model. Separate FEM and ray-trace codes are used offline to produce the structure and optical models, and the wind model is informed by off-line CFD analyses. Each of the wind, structure, optics and controls blocks are influenced by selected design parameters.

The structural model is imported into Matlab from a FEM that includes the telescope, the pier, and the estimated soil compliance. The first 500 modes are used in this analysis (1000 for vibration analysis in Sec. 5), which is more than is necessary. (Of course, there is no reason to expect most of these modes to be accurate in their details, but the intent is to ensure that the qualitative behaviour and static correction from higher modes is retained.) Unless otherwise noted, structural damping of 0.5% is assumed. The response of the structure to the wind is primarily quasi-static, and thus the dominant influence of the damping is on the achievable mount control bandwidth.

The dominant control loops that influence wind response are the mount control system (MCS), described in detail in [5], and the guider; tip/tilt image motion from a wavefront sensor is fed back to the MCS with roughly 0.1 Hz bandwidth. The closed-loop transfer function to applied torques is shown in Fig. 8. The M1CS does not correct global piston/tip/tilt of M1, but does correct higher order deformations at a bandwidth dependent on the Zernike radial degree;[9] unless otherwise noted we use 0.1 Hz for focus, 0.5 Hz for astigmatism, and 1 Hz for higher order modes. Feedback from wavefront focus to M2 despace and coma to M2 decenter are also included in the simulations but have negligible impact on performance due to their low 0.01 Hz bandwidth.

A Zernike decomposition of the OPD is obtained from the linear optical model described in [6]. The image-jitter covariance is used to analytically estimate the PSF, from which the PSS is computed.

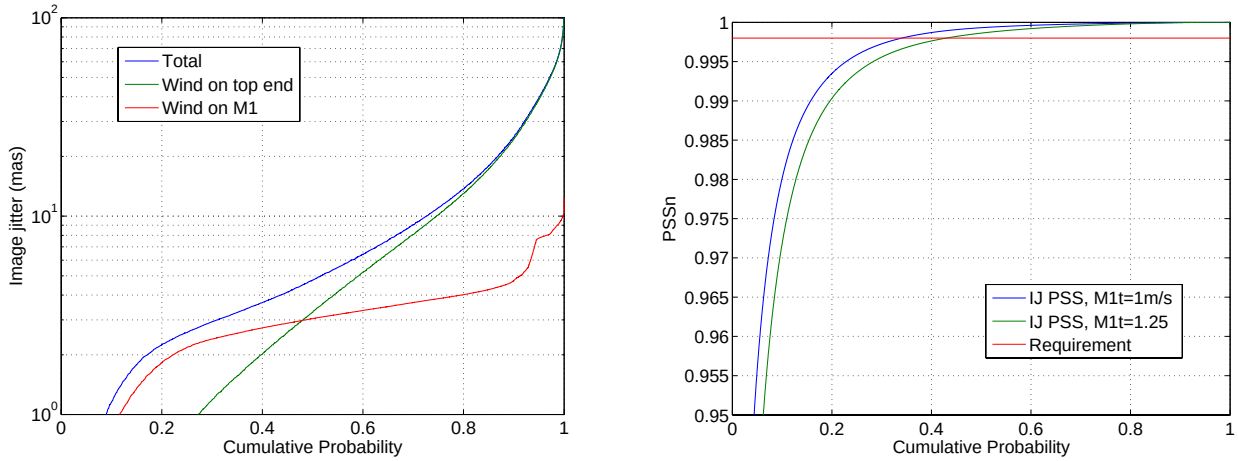

Figure 10. Probability distribution of image jitter response in mas (left) and corresponding contribution to PSS (right). The left-hand plot also shows the breakdown of contributions due to wind loads on M1 and the top end. The contribution due to wind loads on M1 is relatively constant, due to the strategy of maintaining a constant wind speed on M1. The M1 contribution is the larger roughly 45% of the time, but the contribution from the top end dominates the mean and rms image jitter. The contribution to PSS is over-estimated because the correlation between external wind speed and atmospheric seeing is ignored in generating this figure.

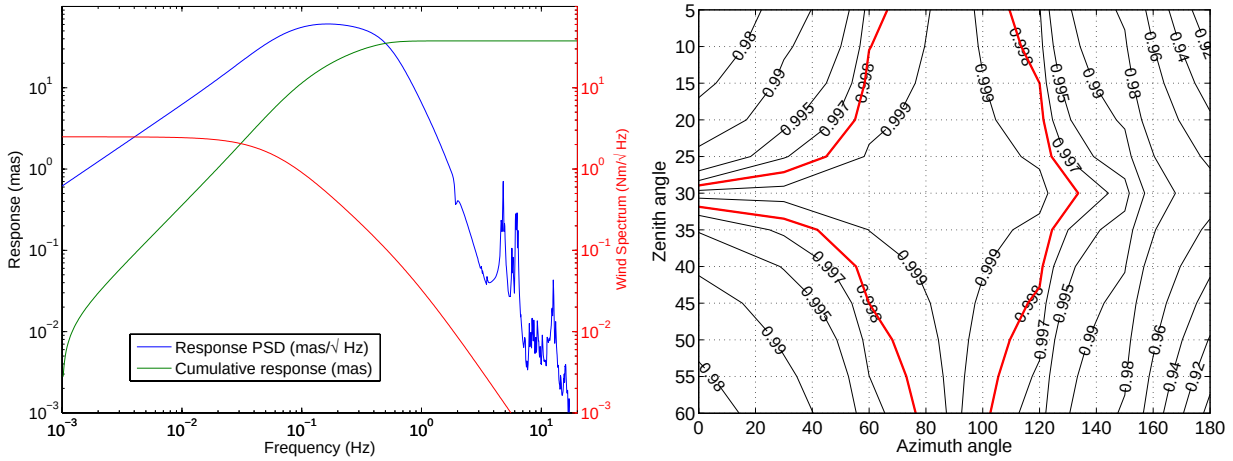

Figure 11. (left) Spectrum of image jitter response, conditions as in Table 1. The response spectrum, cumulative (integrated) response, and wind spectrum are shown. Most of the response is due to disturbances in the 0.1–0.6 Hz band. Right: orientation dependence of PSS at 10 m/s external wind speed and r_0=0.20.

3.2 TMT wind-induced image jitter prediction

The model just described is used to predict the image jitter and aberrations due to the wind loads described in Sec. 2. The image blur due to low order deformation of M1 and dynamic optics misalignment is captured in this model, but provides a negligible contribution to the overall image blur. High-order deformation of M1 will be described in the next section.

The overall performance of interest is plotted in Fig. 10, showing the probability distribution of image jitter and corresponding PSS for a target M1 wind speed of 1 m/s, and the breakdown by source (wind on M1, on top end). Further understanding of the wind effects is described by Fig. 11. The spectrum indicates that most of the response is due to wind loads in the 0.1–0.6 Hz range (where the elevation mount control appears "soft"). The orientation dependence indicates that the best observing strategy at high wind speeds (as shown) is to point at 90° with respect to the wind. The telescope response to wind loads is significantly lower when the forces are not producing significant torques about the elevation axis.

The median, mean, and 85th percentile wind image jitter is 5, 10 and 18 mas respectively, corresponding to PSSn performance of 0.9993, 0.9919, and 0.9892. The PSSn performance estimates are conservative, as they neglect the correlation between atmospheric r_0 and external wind speed. Decreasing the structural damping ratio to 0.0025 reduces the achievable MCS bandwidth f_c by 6%. The image jitter scales with $f_c^{-2.5}$ [5]; this would result in a 16% increase. Changing the M1CS bandwidth does not appreciably affect any of the results. The effect of increasing the target M1 wind speed to 1.25 m/s is also shown in Fig. 10; the image jitter PSSn median, mean, and 85th percentile become 0.9986, 0.9883, and 0.9844. Including an observing strategy whereby observing is reduced in orientations where the dome provides poor shielding of the top-end while the external wind speed is high can reduce the worst-case tail of the predicted image jitter pdf slightly.

3.3 Enclosure wind response

The response to unsteady wind forces on the telescope enclosure is shown in Fig. 12, computed by applying the pier motion from Sec. 2.5 to the integrated model. For a 10 m/s external wind, the response is less than 1 mas. The image motion due to wind loads on the telescope itself at this wind speed average 20 mas, and hence the loads on the enclosure itself can be ignored. The soil transmissibility at Mauna Kea is 10 times larger than at Armazones, but the response to enclosure wind loads would still not be dominant.

4. M1 DYNAMIC SEGMENT RESPONSE

4.1 Modeling

An accurate assessment of the higher order response of the primary mirror is complicated both by the need to apply forces at many more points than are necessary for predicting telescope image motion, and the need to capture the spatial correlation effects to a high degree of accuracy. We therefore use a separate model dedicated to predicting these effects, although many subroutines are shared between models. The basic approach used is similar to that used in simulating performance of AO systems. A pressure screen is generated (similar to the AO phase screen) that has the correct 2-D von Karman spatial statistics, and this screen is propagated in the time domain across M1. At each time step, the force and moments on each segment are computed, and the segment responses due to structure and control system dynamics are obtained. In order to obtain a reasonable assessment of performance, many different random seeds for the pressure screen are required.

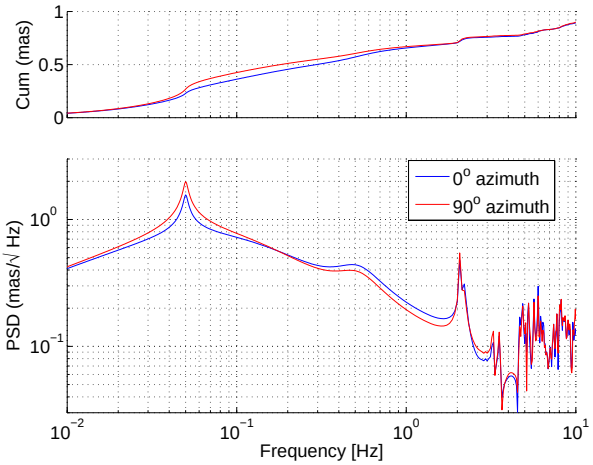

Figure 12. PSD and cumulative PSD (upper) of image motion due to wind forces on the telescope enclosure, using estimated soil properties for Armazones and an external wind speed of 10 m/s. Responses for upwind and 90° to external wind are shown.

The telescope structural dynamics do not significantly affect the wind response, and therefore for simplicity only the static compliance of the structure is used. The dynamics of segment actuator servo loops, however, are important. TMT has not yet selected the actuators that will be used in the primary mirror control system, however one leading candidate is a soft voice-coil actuator stiffened through an active servo control loop.[12] The telescope structural dynamics limit the bandwidth of this servo so that above 1 Hz the actuator is less stiff; these characteristics are taken into account in this model. The global control system is not modeled in detail, however we expect that the control bandwidth will depend on the Zernike mode with lower bandwidth used for lower modes as noted earlier. Because the residual segment rotation (that determines seeing-limited performance) and inter-segment edge discontinuities (that determines AO performance) are both dominated by high-order deformations, the reduction in bandwidth on low order modes does not have a significant affect on performance.

Inputs into the model include the relevant outer scale and turbulent energy fraction for the wind turbulence, as in Eq. (1), including the additional contribution from turbulence generated from interaction with the telescope structure itself. The mean and effective M1 wind speed are also important. Note from Fig. 5 that the wind speed is close to the target wind speed much of the time, and thus analysis will concentrate on these conditions.

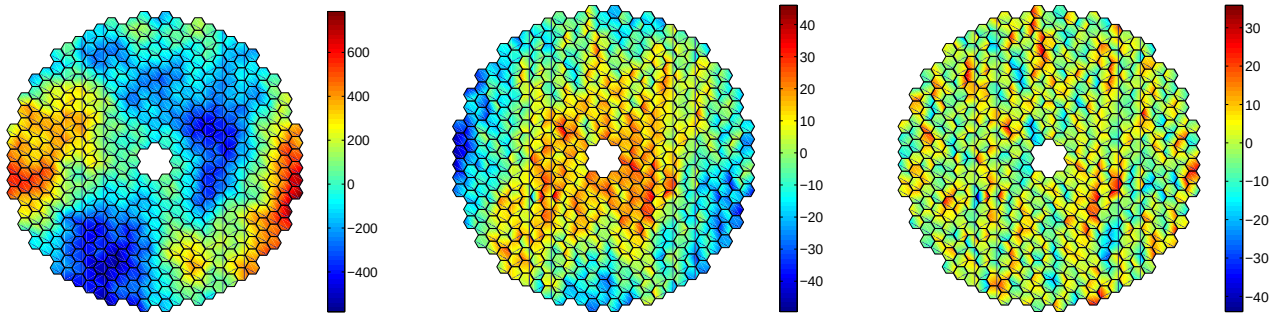

Figure 13. Typical M1 response to 1 m/s wind, in nm. No control (left), with M1CS (centre) and with low wavenumbers removed to estimate residual after AO correction (right). A 1 Hz M1CS bandwidth is used except 0.5 Hz on astigmatism and 0.1 Hz on focus mode. Global piston, tip and tilt are projected out. The residual rms surface response is 223, 14, and 7 nm rms respectively; the latter difference is primarily due to focus and astigmatism.

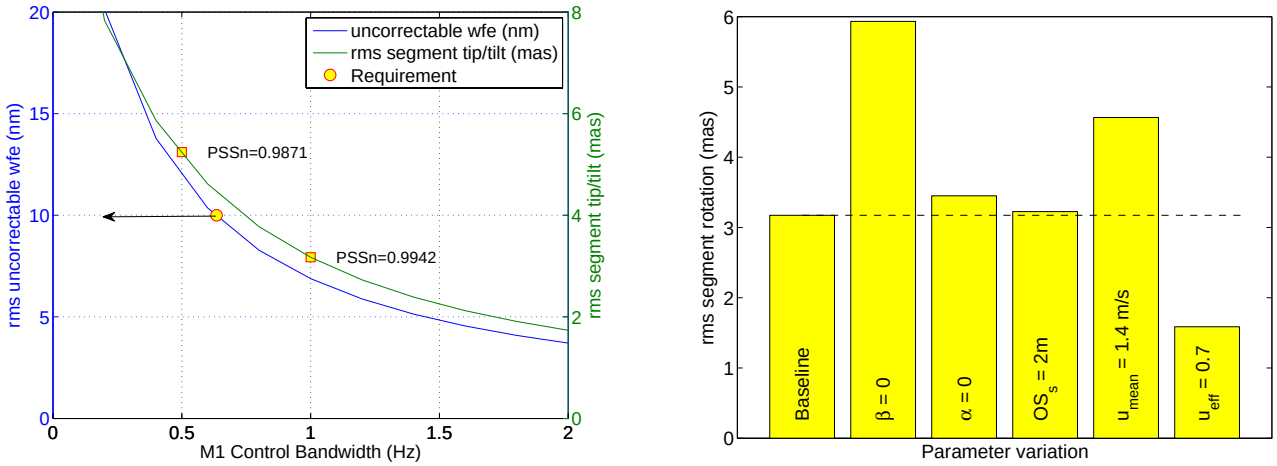

Figure 14. Performance as a function of M1CS bandwidth (left) and as a function of wind parameters (right). Nominal wind parameters used are: mean and rms wind speed of 1 m/s, outer scales of 30, 5, and OS_s=1 m with fractions $\beta = 0.25$, $1 - \alpha - \beta = 0.5$ and $\alpha = 0.25$ of the turbulent energy respectively. Sensitivity is shown for varying β, α, OS_s, mean wind (with u_{eff}=1) and u_{eff} (with $u_{\mathrm{mean}} = 1$).

4.2 Segment response

A typical M1 response map with 1 Hz M1CS bandwidth and 1 m/s M1 wind speed (mean and effective) is shown in Fig. 13. The outer scale is 30 m, 5 m, and 1 m for the three sources of turbulence (aperture, vents, structure), with 25%, 50% and 25% of the turbulent energy respectively.

Figure 14 shows the dependence of both the AO-relevant error and the seeing-limited error as a function of M1CS control bandwidth; both of these are proxy estimates for the actual performance calculations. The relevant performance metric for AO is 10 nm rms uncorrectable wavefront error; we assume the AO corrects all low-order and 50% of the high-order aberrations (this has been validated through AO simulations). This is achieved for the choice of wind parameters in Fig. 14 at an M1CS bandwidth ~ 0.65 Hz. However, the high-order segment dynamic response has a greater contribution to the normalized PSS than would be expected from the small rms segment tip/tilts and does not meet the desired error budget at a 1 Hz bandwidth (although at 0.9942 it is acceptable), and significantly exceeds the budget at 0.5 Hz (PSSn = 0.9871, which would be unacceptable).

The dependence of performance on input assumptions is also shown in Fig. 14, where outer scales and wind speeds are changed for a fixed control bandwidth to assess the range of variability and uncertainty in the performance estimates. Only the rms segment rotation sensitivity is shown; the rms surface sensitivity is similar. Changes in the mean and effective wind speeds result in a significant shift in performance. The turbulence due to the aperture is of sufficiently long length scale to have minimal impact, and the total response is proportional to the amplitude of smaller-scale turbulence. The additional turbulence introduced to simulate the interaction with the telescope structure does not significantly change the performance.

	Image Motion (mas/N)			rms WFE (nm/N)		
Location	5–15 Hz	15–25 Hz	25–35 Hz	5–15 Hz	15–25 Hz	25–35 Hz
M2	0.8	0.16	0.08	13	4.5	*0.9*
M3	1.0	0.04	0.01	24	8	*2*
Nasmyth platform	0.3	0.01	0.001	5	0.5	*0.04*
Laser enclosure	0.09	0.01	0.01	2	0.9	*0.3*
Pier (response/nm)	0.13	0.03	0.05	5	3.6	*1.1*

Table 2. TMT vibration response as a function of frequency and source location. Tip/tilt in mas/nm for pier vibration and mas/N at other locations, and rms tip-tilt-removed wavefront error in nm/nm for pier and nm/N at other locations. The 25–35 Hz wavefront error column does not account for the amplification due to the M1 segment resonances.

5. VIBRATION AND ACOUSTICS

5.1 Vibration

While equipment vibration is an important source of dynamic response for TMT, much less can currently be quantified than for wind. Vibration is known to be an issue at the Keck observatories, for example, with narrowband tones 29-30 Hz in particular being a problem. Most of the residual wind response is at frequencies well below the AO control bandwidth, and so any motion that is spatially correctable by AO can be corrected. However, this is not true for equipment vibration, due to the higher temporal frequencies.

Our strategy is twofold; to analyze the propagation of disturbances from relevant points on the structure to the optical line-of-sight (LOS) and wavefront error (WFE) in order to place specifications on the allowable source amplitudes, and to use measured vibration amplitudes to assess whether these specifications are plausible, given best engineering practices on source mitigation (choosing low-vibration equipment, locating it away from the telescope, and isolating it from the foundation).

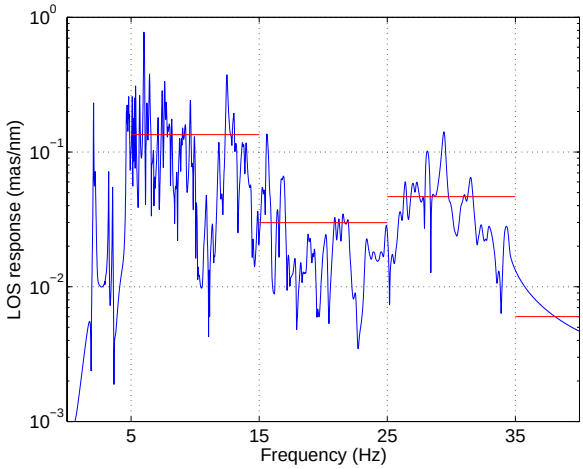

Figure 15. Rms LOS due to pier vibration (rms over x, y and z motion), and rms response in frequency bands.

Vibrations are applied to the telescope integrated model at locations listed in Table 2. For each location, the resulting image motion is averaged over both axes, averaged over the x, y, and z components of vibration, and averaged over 10 Hz frequency bands to give the response estimates quoted in the Table. A representative frequency response, for pier vibration, is shown in Fig. 15. Representative amplitudes for pier vibration are computed in [8] for hypothetical isolated rotating machinery located on the mountaintop and transmitting vibration through the soil. For example, a large chiller could produce ∼1.6 nm of pier motion at high frequencies. The resulting ∼0.1 mas image motion and 2 nm higher-order wavefront error would both be significant relative to the error budgets of 1 mas and 10 nm, but suggest that the budget is not unrealistic.

5.2 Acoustics

Acoustic pressure sources within the telescope enclosure could include both narrowband tones from equipment (similar to vibration but propagated acoustically rather than mechanically), and also broadband energy radiated from the high-intensity turbulence in the shear layer above the enclosure aperture. These forces differ from the turbulent wind pressure forces both in their source, and in the propagation speed and therefore spatial correlation; these are pressure waves propagating at the speed of sound rather than the pressure resulting from local turbulence convected at the mean wind speed. At low frequencies the resulting correlation length is such that the forces on the front and back side of the primary mirror will cancel (this is effectively true at all relevant frequencies for other optics). However, the wavelength approaches that of the mirror above 10 Hz, and it is possible for acoustic forces above this frequency to result in appreciable deformation of M1. The observation that observatories are "quiet" constrains the possible acoustic amplitudes to unimportant levels above ∼40 Hz where they would otherwise be audible, but between 10 and 40 Hz amplitudes of ∼70 dBSPL are possible (re 20μPa), hence 0.07 Pa or 0.1 N per segment.

The servo bandwidth for an M1CS voice-coil actuator is constrained to be less than roughly 20 Hz,[12] leading to a compliance as high as 1 μm/N in the 15-25 Hz range and response therefore of 100 nm. This would be correlated across many segments and thus does not have significant seeing-limited consequences, but for an AO bandwidth of only 30 Hz, the post-correction residual of 50-65 nm would be excessive. A similar issue exists for a stiff M1CS actuator due to the resulting undamped segment resonance; any acoustic disturbances in the frequency region of the segment resonances ($\sim$35 Hz) will lead to significant mirror response. Measurements are being planned for Keck to quantify the acoustic environment; until data is available, the best quantification only allows us to acknowledge that this could be an important error term to track for AO observations in particular.

6. CONCLUSIONS

The response of the Thirty Meter Telescope to modeled dynamic disturbance sources is within desired error targets. Wind influences the telescope through forces on the top-end and upper telescope structure, forces on the primary mirror, and forces on the enclosure. The latter of these is the smallest contributor. Relevant contributions include both image motion from unsteady torques about the elevation axis, and higher-order deformations from M1 segment motion. The mean contribution to PSS performance from these is 0.9919 and 0.9942 respectively. These performance estimates are sensitive to a variety of assumptions, with the most significant being (i) the target wind speed on M1 obtained from venting, and (ii) the structural damping that results in constraints on control bandwidths (MCS and M1CS).

Other dynamic disturbances on TMT include equipment vibration and acoustic forces. Specifications are presented on source amplitudes for equipment vibration that lead to acceptable response and are believed to be realistically achievable. Acoustic force amplitudes are unknown but can be reasonably bounded to a level that, while relevant, is not unacceptable.

Additional data on both acoustic and vibration amplitudes is being obtained from measurements at Keck Observatories in order to further refine these estimates. Additional validation of expected wind loads will be obtained from a wind tunnel test conducted with the current enclosure and telescope design. Once a site has been selected, soil modulus measurements will be fed into the structural modeling.

Appendix: Frozen turbulence decorrelation calculation

Here we derive the frequency-dependent effects of spatial decorrelation of turbulence to obtain the force spectrum. The analysis for a Zernike-decomposition of M1 forces is given in [7].

Most of the structural members of the upper telescope are long and thin, so decorrelation is only relevant over one dimension of length L. For simplicity, consider wind speed U orthogonal to the structure, and arbitrarily label this the x-axis. We want to know the net force on the structure as a function of frequency, assuming von Karman pressure statistics and frozen turbulence.

At a given wavenumber k_y, the force is the integral of the sinusoidally varying pressure along the structure

$$F = \int_{-L/2}^{L/2} p(y)\mathrm{d}y \qquad \Rightarrow \qquad F(k_y) = L|p(k_y)|\frac{\sin k_y L}{k_y L}$$

The amplitude of the pressure is obtained from the 2-D von Karman pressure spectrum

$$\Phi_p^{2\mathrm{D}}(k) = \left(\frac{1}{1+(k/k_0)^2}\right)^{10/6}$$

with wavenumber $k = (k_x^2 + k_y^2)^{1/2}$. Frozen turbulence relates the temporal frequency to the wavenumber in the wind direction, $k_x = f/U$. The total contribution at frequency f is obtained by integrating over all possible wavenumbers k_y in the orthogonal direction. Thus

$$\Phi_F(f) = L^2 \int_0^\infty \Phi_p^{2\mathrm{D}}(k) \left[\frac{\sin k_y L}{k_y L}\right]^2 \mathrm{d}k_y \qquad (2)$$

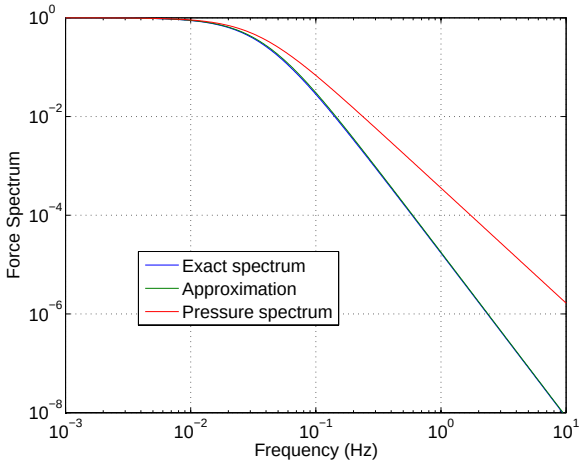

Figure 16. Comparison of exact integral and fit for the normalized force spectrum on a structure of length L perpendicular to the wind, and comparison with normalized pressure spectrum. The outer scale used was $L_0 = 30$ m, structure length $L = 10$ m and wind speed $U = 1$ m/s.

The integral can be performed numerically. The overall temporal force spectrum that results from (2) can reasonably be approximated by the product of the 1-D von Karman pressure spectrum with corner frequency set by the turbulence outer scale, and an additional attenuation factor with corner frequency that is a function of the spatial length scale of the structure. Both factors involve the same convective velocity to scale between spatial and temporal frequencies. Therefore, if one is considering structures which are small compared to the outer scale of turbulence, one can ignore the structural spectral factor.

The structural attenuation factor (on the power spectrum, not the amplitude spectrum) that is used in the fit shown in Fig. 16 is

$$\frac{1}{\sqrt{1+(f/f_s)^2}} \qquad \text{with} \qquad f_s = \frac{U}{2L}$$

The high frequency attenuation relative to the pressure spectrum is a factor

$$n = \frac{2Lf}{U} = \frac{L}{\lambda/2}$$

(a factor of $\sqrt{n}$ in amplitude). This is equivalent to the force resulting from n independent turbulent structures that add in quadrature, where the correlation length that defines n is half the wavelength $\lambda = U/f$.

Acknowledgements

The TMT Project gratefully acknowledges the support of the TMT partner institutions. They are the Association of Canadian Universities for Research in Astronomy (ACURA), the California Institute of Technology and the University of California. This work was supported as well by the Gordon and Betty Moore Foundation, the Canada Foundation for Innovation, the Ontario Ministry of Research and Innovation, the National Research Council of Canada, the Natural Sciences and Engineering Research Council of Canada, the British Columbia Knowledge Development Fund, the Association of Universities for Research in Astronomy (AURA) and the U.S. National Science Foundation.

REFERENCES

1. Seo, B.-Y., Nissly, C. R., Angeli, G. Z., Ellerbroek, B. L., Nelson, J. E., Sigrist, N., and Troy, M., "Analysis of Point Source Sensitivity as a performance metric for the Thirty Meter Telescope," *Proc. SPIE*, 2008. SPIE 7017-28.
2. Vogiatzis, K. and Angeli, G. Z., "Monte Carlo Simulation Framework for TMT," *Proc. SPIE*, 2008. SPIE 7017-29.
3. MacMynowski, D. G., Blaurock, C., Angeli, G. Z., and Vogiatzis, K., "Modeling wind-buffeting of the Thirty Meter Telescope," *Proc. SPIE*, 2006. SPIE 6271-25.
4. Szeto, K., Roberts, S., Gedig, M. H., Lagally, C., Tsang, D., MacMynowski, D. G., Sirota, M. J., Stepp, L. M., and Thompson, P. M., "TMT telescope structure system: design and development progress report," *Proc. SPIE*, 2008. SPIE 7012-88.
5. Thompson, P. M., MacMynowski, D. G., and Sirota, M. J., "Analysis of the TMT Mount Control System," *Proc. SPIE*, 2008. SPIE 7012-60.
6. Angeli, G. and Gregory, B., "Linear Optical model for a large ground based telescope," *Proc. SPIE*, Vol. 5178, 2003, pp. 64–73.
7. MacMynowski, D. G., Vogiatzis, K., Angeli, G. Z., Fitzsimmons, J., and Nelson, J., "Wind Loads on Ground-Based Telescopes," *Applied Optics*, Vol. 45, No. 30, pp. 7912–7923, 2006.
8. Sagals, G., MacMynowski, D. G., and Vogiatzis, K., "Finite element analysis of TMT vibrations transmitted through telescope-enclosure-soil interaction," *Proc. SPIE*, 2008. SPIE 7017-73.
9. MacMynowski, D. G., Thompson, P. M., and Sirota, M. J., "Analysis of TMT Primary Mirror Control-Structure Interaction," *Proc. SPIE*, 2008. SPIE 7017-41.
10. Andersen, T. E., Enmark, A., Linde, P., Owner-Petersen, M., Sjstrm, A., Koch, F., Mller, M., Noethe, L., and Sedghi, B., "An integrated model of the European ELT," *Proc. SPIE*, 2008. SPIE 7017-27.
11. Vogiatzis, K., "Advances in aero-thermal modeling for TMT," *Proc. SPIE*, 2008. SPIE 7017-25.
12. Thompson, P. M., MacMynowski, D. G., and Sirota, M. J., "Control Analysis of the TMT Primary Segment Assembly," *Proc. SPIE*, 2008. SPIE 7012-58.